


Design and analysis of a triangular bi-axial flexure hinge

Proc IMechE Part C:
J Mechanical Engineering Science
1–14
© IMechE 2023
Article reuse guidelines:
sagepub.com/journals-permissions
DOI: 10.1177/09544062231154836
journals.sagepub.com/home/pic


Jun-wei Lin^{1,2} , Yang Zhao^{1,2} , Qing-wen Wu^{1,2}, Ha-si-ao-qi-er Han¹ ,
Peng Yu¹ and Yang Zhang²

Abstract

To achieve the requirement of flexure hinges for specific optical precision equipment, a new triangular bi-axial flexure hinge is proposed. The analysis model for the flexibility of the triangular bi-axial flexure hinges is derived. After that, the linear and nonlinear finite element methods are used to verify the analysis model. Then, the physical dimensions of the hinge are optimized using the multi-island genetic algorithm in conjunction with the finite element method, and the rotational stiffness and center drift are diminished. Static analysis and modal analysis of the hinge are conducted. A test system was built to gage the flexure hinge's rotational stiffness. The results demonstrated that there was good agreement between the analytically calculated value, simulated calculated value, and experimental value. To summarize, the analysis model met the design requirements of the triangular bi-axial flexible hinge, and the multi-island genetic algorithm effectively optimized the physical dimensions of the hinge and enhanced its performance. The design process provides new ideas for the design of other forms of hinges.

Keywords

Triangular bi-axial flexure hinge, finite element simulation, dimension optimization, multi-island genetic algorithm, rotational stiffness

Date received: 1 November 2022; accepted: 18 January 2023

Introduction

When used as connecting parts to transfer force and motion, traditional rigid hinges generate rotational motion using the relative rotation between the rotating shaft and the support. However, because of the presence of clearance in the rigid hinge, problems such as friction and lubrication steadily emerge when the hinge is used in high-precision scenarios, which places a higher demand on lubricants, while also weakening the hinge's service life and increasing maintenance costs. Friction wear also reduces hinge performance and has a direct effect on transmission accuracy. When subjected to torsional force, a flexure hinge is a unique kinematic pair that uses material deformation to generate displacement and produces rotary motion around its center of rotation within a limited angle range. It has several advantages over standard rigid hinges, such as no return stroke, no friction, no gap, no noise, no wear, a small size, high motion sensitivity, and steady motion.^{1–4} Therefore, flexure hinges are used in many devices, such as a mirror mount,^{5,6} positioning-vibration isolation stage,⁷ piezoelectric stick slip actuator,^{8,9} micro-positioning stage,^{10–12} and accelerometer.¹³

Flexure hinges can be categorized as single-axis, double-axis, or multi-axis based on the number of

rotational axes and the functions used.¹⁴ Single-axis flexure hinges include the cycloidal hinge,¹⁵ straight beam-type hinge,¹⁶ and annulus-shaped hinge.¹⁷ Double-axis hinges include the notch U joint¹⁸ and compliant Cardan U joint.¹⁹ Multi-axis hinges include multiple-axis flexure hinges²⁰ and the CS joint.²¹ Additionally, according to the cross-sectional geometry of flexure units, hinges can be classified into the regular type (e.g. elliptical hinge, straight beam hinge, parabolic hinge, and cycloidal hinge) and composite type (e.g. cartwheel hinge, straight beam-straight circle hinge, straight circle-elliptical hinge).

Because stress is dispersed throughout the length of the entire straight beam when it is loaded, the straight beam-type flexure hinge has a wide range of rotation.²² In recent years, scholars have conducted in-

¹Changchun Institute of Optics, Fine Mechanics and Physics, Chinese Academy of Sciences, Changchun, China

²University of Chinese Academy of Sciences, Beijing, China

Corresponding author:

Yang Zhao, Changchun Institute of Optics, Fine Mechanics and Physics, Chinese Academy of Sciences, No. 3888, Dong Nanhu Road, Changchun 130033, China.
Email: zhaoyang9185@163.com

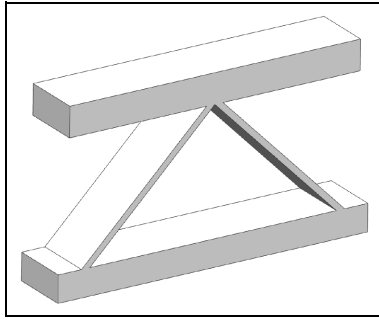


Figure 1. Triangular flexure hinge.

depth research on it. Some scholars have investigated the hinge itself. Lobontiu et al.²³ established the stiffness model of the straight beam-type flexure hinge based on Castigliano's second theorem and analyzed its rotation accuracy. In the Framework of Screw Theory, Yu et al.²⁴ analyzed the constraint fundamental building blocks (FBBs) equivalent and equivalent freedom FBBs for the straight beam-type flexure hinge. Dirksen and Lammering²⁵ derived analytical expressions for the displacement and stress of the hinge and verified the results through a numerical simulation and experiments. Shusheng et al.²⁶ analyzed the deformation properties of the straight beam-type flexure hinge. Mahto²⁷ developed an optimization model using the Lagrange finite element method (FEM) and investigated the design optimization problem of the hinge. Other scholars have designed new types of hinges based on straight beam-type flexure hinges. Pei et al.²⁸ combined two beams with two rigid bodies to form the leaf-type isosceles-trapezoidal flexural hinge, which has the characteristics of a large stroke and small stiffness. Ling et al.²⁹ derived the dynamic stiffness matrix, which depends on the frequency of the flexure beam. Chen et al.³⁰ created a hinge with damping layers using a strain energy approach and the Kelvin damping model, which effectively reduced vibration. Based on the X-lattice structure, Zhang et al.³¹ designed a new structure for the beam flexure hinge. Awatar et al.³² simplified the cantilever beam stress-strain model to facilitate the design of reed-type flexure hinges. Li and Hao³³ proposed the nonlinear spatial model of anti-buckling universal joint consisting of two inversion-based symmetric crossspring pivots.

The triangular flexure hinge (Figure 1) is a single-axis composite hinge with its center of rotation at the junction of two straight beams. It consists of two straight beam-type flexure hinges that are placed on the same plane. This type of flexure hinge has the benefits of large corner travel, small center drift, high rotational accuracy, strong yield resistance, and easy processing and assembly. A triangular bi-axial flexure hinge with the same stiffness in two orthogonal directions is formed using Wire cut Electrical Discharge

Machining (WEDM) to process a hollow cylinder in orthogonal directions. This form of bi-axial flexure hinge has the following advantages: (1) The rotational rigidities in orthogonal directions are equal, and the axial and torsional rigidities are higher. (2) WEDM is used for integrated processing; hence, so there is no need for assembly.³⁴

In this study, to achieve the requirement of flexure hinges for specific optical precision equipment, a new triangular bi-axial flexible hinge is proposed and investigated. This paper is organized as follows: In Section 2, the analysis model for the flexibility of the triangular bi-axial flexure hinge is derived. Then, the relationship between rotational stiffness and the hinge parameters is analyzed. In Section 3, the linear and nonlinear finite element methods are used to verify the analysis model, the designed hinge is compared with the cross-axis bi-axial hinge. In Section 4, the physical dimensions of the hinge are optimized using the multi-island genetic algorithm in conjunction with the FEM. In Section 5, static analysis and modal analysis of the hinges are conducted. In Section 6, a test system that was built to verify the correctness of the analysis and design is described. Finally, in Section 7, the study is summarized.

Triangular bi-axial flexure hinge analysis model

Flexure hinges for specific optical precision equipment require more flexibility in the direction of motion and less flexibility in the non-motion direction. Four completely consistent triangular flexure hinges with rotational flexibility are formed by performing WEDM on the hollow cylinder, thereby providing constraints for rotation around two axes. The designed triangular bi-axial flexure hinge is shown in Figure 2.

Single straight beam hinge

The reeds of straight beam-type hinges can be regarded as cantilever beams because they are a composite of straight beam-type flexure hinges that make up the triangular flexure hinge. Based on von Mises theory and screw theory, Selig and Ding³⁵ deduced the elastic model of the cantilever beam. When a load is applied to the end of a homogeneous beam, the end of the beam is deformed or moves slightly. According to the screw theory, in the coordinate system shown in Figure 3, the deformation at the end of the beam can be represented by the motion screw T ; the load applied to the end of the beam can be represented by the force screw W .

$$T = (\theta_x \ \theta_y \ \theta_z \ d_x \ d_y \ d_z)^T \quad (1)$$

$$W = [M_x \ M_y \ M_z \ F_x \ F_y \ F_z]^T \quad (2)$$

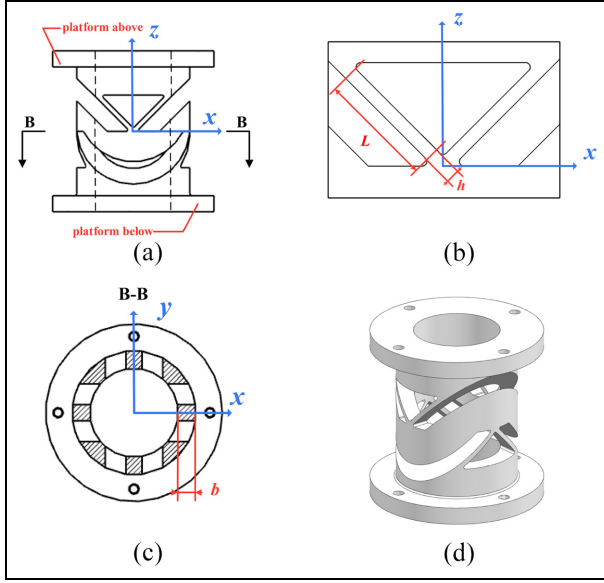


Figure 2. Designed triangular bi-axial flexure hinge: (a) front view of the hinge, (b) partially enlarged view of the hinge, (c) top sectional view of the hinge, and (d) positive tri-axial view of the hinge.

In equation (1), θ and d represent the angular deformation and linear deformation at the end of the beam, respectively. In equation (2), M and F represent the torques and forces applied to the beam. Under the condition of linear elasticity and small displacement, the relationship between the motion screw and the force screw is as follows:

$$T = CW, W = KT, C = K^{-1} \quad (3)$$

In equation (3), C represents the flexibility matrix of the cantilever beam, K represents the stiffness matrix of the cantilever beam.

According to the von Mises theory, the flexibility matrix when the force spin is applied to the end of the cantilever beam is:

$$C = \begin{bmatrix} c_{\theta_x-M_x} & 0 & 0 & 0 & c_{\theta_x-F_y} & 0 \\ 0 & c_{\theta_y-M_y} & 0 & c_{\theta_y-F_x} & 0 & 0 \\ 0 & 0 & c_{\theta_z-M_z} & 0 & 0 & 0 \\ 0 & 0 & 0 & c_{d_x-F_y} & 0 & 0 \\ 0 & 0 & 0 & 0 & c_{d_y-F_x} & 0 \\ 0 & 0 & 0 & 0 & 0 & c_{d_z-F_z} \end{bmatrix} \quad (4)$$

Where:

$$\begin{aligned} c_{\theta_x-M_x} &= \frac{12L}{Ehb^3} & c_{\theta_x-F_y} &= c_{d_y-M_x} = -\frac{6L^2}{Ehb^3} \\ c_{\theta_y-M_y} &= \frac{12L}{Ebh^3} & c_{\theta_y-F_x} &= c_{d_x-M_y} = \frac{6L^2}{Ebh^3} \\ c_{\theta_z-M_z} &= \frac{24(1+\nu)L}{E(hb^3+bh^3)} & c_{d_x-F_y} &= \frac{4L^3}{Ebl^3} \\ c_{d_y-F_x} &= \frac{4L^3}{Ehb^3} & c_{d_z-F_z} &= \frac{L}{Ehb} \end{aligned} \quad (5)$$

L and b are the length and width of the beam, respectively; E is the modulus of elasticity of the material; ν is the Poisson's ratio of this material; and h is the height of the beam.

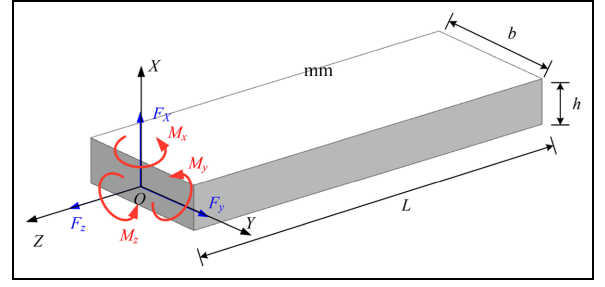


Figure 3. Mechanical model of the cantilever beam.

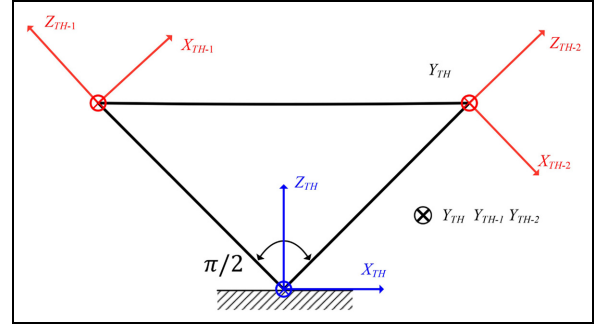


Figure 4. Force model of the triangular flexure hinge.

The triangular flexure hinge

For the triangular flexure hinge, it is formed by orthogonal parallel connection of two straight beam hinges. The local coordinate systems $O_{TH-1} - X_{TH-1} Y_{TH-1} Z_{TH-1}$ and $O_{TH-2} - X_{TH-2} Y_{TH-2} Z_{TH-2}$ are established at the end of the straight beam type hinge, the reference coordinate system $O_{TH} - X_{TH} Y_{TH} Z_{TH}$ is established at the vertex of the triangle, as shown in Figure 4.

The rotation matrix of the local coordinate systems $O_{TH-1} - X_{TH-1} Y_{TH-1} Z_{TH-1}$ and $O_{TH-2} - X_{TH-2} Y_{TH-2} Z_{TH-2}$ transformed with the reference coordinate system $O_{TH} - X_{TH} Y_{TH} Z_{TH}$ is R_{TH} .

$$R_{TH} = R_{THX} R_{THY} R_{THZ} \quad (6)$$

R_{THX} , R_{THY} , R_{THZ} represent the rotational matrixes around X_{TH} , Y_{TH} , and Z_{TH} , respectively, as shown in equation (7):

$$\begin{aligned} R_{THX} &= \begin{bmatrix} 1 & 0 & 0 \\ 0 & \cos\theta_{THX} & \sin\theta_{THX} \\ 0 & \sin\theta_{THX} & \cos\theta_{THX} \end{bmatrix} \\ R_{THY} &= \begin{bmatrix} \cos\theta_{THY} & 0 & \sin\theta_{THY} \\ 0 & 1 & 0 \\ -\sin\theta_{THY} & 0 & \cos\theta_{THY} \end{bmatrix} \\ R_{THZ} &= \begin{bmatrix} \cos\theta_{THZ} & -\sin\theta_{THZ} & 0 \\ \sin\theta_{THZ} & \cos\theta_{THZ} & 0 \\ 0 & 0 & 1 \end{bmatrix} \end{aligned} \quad (7)$$

The translation vector of the local coordinate systems $O_{TH-1} - X_{TH-1}Y_{TH-1}Z_{TH-1}$ and $O_{TH-2} - X_{TH-2}Y_{TH-2}Z_{TH-2}$ with the reference coordinate system $O_{TH} - X_{TH}Y_{TH}Z_{TH}$ is t_{TH} .

$$t_{TH} = (x_{TH}, y_{TH}, z_{TH}) \quad (8)$$

The antisymmetric matrix of the translation vector is:

$$T_{TH} = \begin{bmatrix} 0 & -z_{TH} & y_{TH} \\ z_{TH} & 0 & -x_{TH} \\ -y_{TH} & x_{TH} & 0 \end{bmatrix} \quad (9)$$

The accompanying matrix Ad_{TH} of the coordinate transformation is:

$$Ad_{TH} = \begin{bmatrix} R_{TH} & 0_{3 \times 3} \\ T_{TH}R_{TH} & R_{TH} \end{bmatrix}_{6 \times 6} \quad (10)$$

where $0_{3 \times 3}$ is a third-order zero matrix.

For the straight beam flexure hinges 1 and 2, the coordinate transformation satisfies:

$$\begin{aligned} R_{TH-1} &= R_{THX}(0)R_{THY}\left(-\frac{\pi}{4}\right)R_{THZ}(0) \\ t_{TH-1} &= (-l\sin\left(\frac{\pi}{4}\right) \quad 0 \quad l\cos\left(\frac{\pi}{4}\right)) \end{aligned} \quad (11)$$

$$\begin{aligned} R_{TH-2} &= R_{THX}(0)R_{THY}\left(\frac{\pi}{4}\right)R_{THZ}(0) \\ t_{TH-2} &= (l\sin\left(\frac{\pi}{4}\right) \quad 0 \quad l\cos\left(\frac{\pi}{4}\right)) \end{aligned} \quad (12)$$

For the triangular flexure hinge, it is made of two straight type flexure hinges orthogonally connected in parallel, so its flexibility matrix C_{TH} is:

$$C_{TH} = \left((Ad_{TH-1}CA_{TH-1}^T)^{-1} + (Ad_{TH-2}CA_{TH-2}^T)^{-1} \right)^{-1} \quad (13)$$

Substituting equations (4), (10), (11), and (12) into equation (13), the flexibility matrix of the triangular flexure hinge C_{TH} can be calculated as follows:

$$C_{TH} = \begin{bmatrix} c_{TH-11} & 0 & 0 & 0 & c_{TH-15} & 0 \\ 0 & c_{TH-22} & 0 & c_{TH-24} & 0 & 0 \\ 0 & 0 & c_{TH-33} & 0 & 0 & 0 \\ 0 & c_{TH-42} & 0 & c_{TH-44} & 0 & 0 \\ c_{TH-51} & 0 & 0 & 0 & c_{TH-55} & 0 \\ 0 & 0 & 0 & 0 & 0 & c_{TH-66} \end{bmatrix} \quad (14)$$

Where:

$$c_{TH-11} = \frac{24(L + Lv)}{Ebh(2b^2v + 3b^2 + h^2)} \quad (15)$$

$$c_{TH-15} = c_{TH-51} = \frac{6L^2(\sqrt{2}v + \sqrt{2})}{Ebh(2b^2v + 3b^2 + h^2)} \quad (16)$$

$$c_{TH-22} = \frac{6(L^3 + Lh^2)}{Ebh(4L^2h^2 + h^4)} \quad (17)$$

$$c_{TH-24} = c_{TH-42} = -\frac{3\sqrt{2}L^2}{Ebh(4L^2 + h^2)} \quad (18)$$

$$c_{TH-33} = \frac{24(L + Lv)}{Eb(9b^2h + h^3 + 8b^2hv)} \quad (19)$$

$$c_{TH-44} = \frac{4L^3}{Ebh(4L^2 + h^2)} \quad (20)$$

$$c_{TH-55} = \frac{L^3(8b^2v + 9b^2 + h^2)}{2Eb^3h(2b^2v + 3b^2 + h^2)} \quad (21)$$

$$c_{TH-66} = \frac{L^3}{Eh(bL^2 + bh^2)} \quad (22)$$

The triangular bi-axial flexure hinge

The motion and load of the triangular bi-axial flexure hinge is defined at its top center where a global coordinate system $O_{TBH} - X_{TBH}Y_{TBH}Z_{TBH}$ is located as shown in Figure 5(a). The four triangular flexure hinges are numbered, and their corresponding local coordinate systems are denoted as $O_{TBH-1} - X_{TBH-1}Y_{TBH-1}Z_{TBH-1}$, $O_{TBH-2} - X_{TBH-2}Y_{TBH-2}Z_{TBH-2}$, $O_{TBH-3} - X_{TBH-3}Y_{TBH-3}Z_{TBH-3}$, and $O_{TBH-4} - X_{TBH-4}Y_{TBH-4}Z_{TBH-4}$, respectively, as shown in Figure 5(b) and (c).

The rotational matrix of the local coordinate systems $O_{TBH-i} - X_{TBH-i}Y_{TBH-i}Z_{TBH-i}$ transformed with the global coordinate system $O_{TBH} - X_{TBH}Y_{TBH}Z_{TBH}$ is R_{TBH} :

$$R_{TBH} = R_{TBHX}R_{TBHY}R_{TBHZ} \quad (23)$$

R_{TBHX} , R_{TBHY} , and R_{TBHZ} represent the rotational matrixes around X_{TBH} , Y_{TBH} , and Z_{TBH} , respectively, as shown in equation (24).

$$\begin{aligned} R_{TBHX} &= \begin{bmatrix} 1 & 0 & 0 \\ 0 & \cos\theta_{TBHX} & \sin\theta_{TBHX} \\ 0 & \sin\theta_{TBHX} & \cos\theta_{TBHX} \end{bmatrix} \\ R_{TBHY} &= \begin{bmatrix} \cos\theta_{TBHY} & 0 & \sin\theta_{TBHY} \\ 0 & 1 & 0 \\ -\sin\theta_{TBHY} & 0 & \cos\theta_{TBHY} \end{bmatrix} \\ R_{TBHZ} &= \begin{bmatrix} \cos\theta_{TBHZ} & -\sin\theta_{TBHZ} & 0 \\ \sin\theta_{TBHZ} & \cos\theta_{TBHZ} & 0 \\ 0 & 0 & 1 \end{bmatrix} \end{aligned} \quad (24)$$

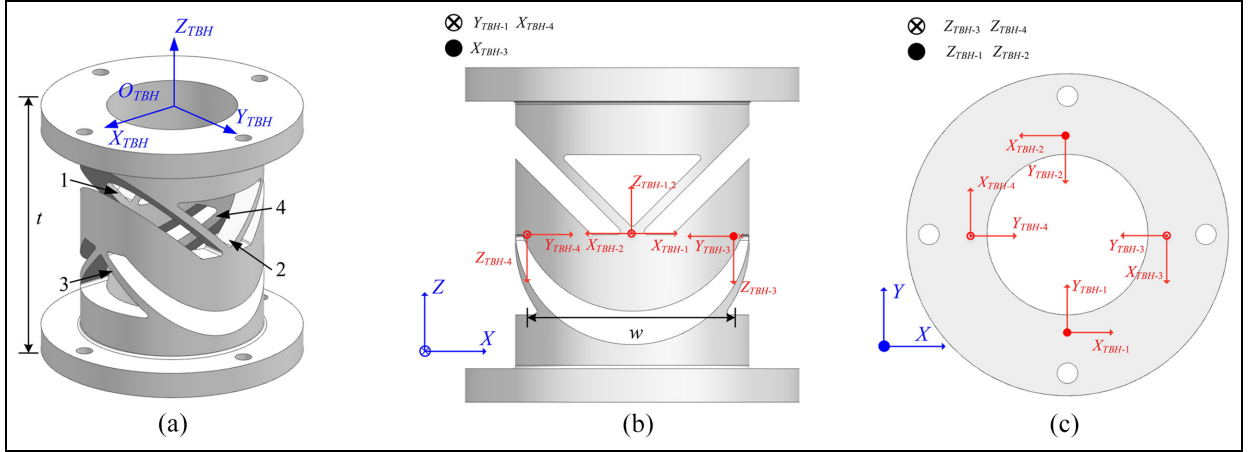


Figure 5. Local coordinate systems and the global coordinate system of the hinge: (a) the global coordinate system $O_{TBH} - X_{TBH} Y_{TBH} Z_{TBH}$, (b) the side view of the local coordinate systems $O_{TBH-i} - X_{TBH-i} Y_{TBH-i} Z_{TBH-i}$, and (c) the top view of local coordinate systems $O_{TBH-i} - X_{TBH-i} Y_{TBH-i} Z_{TBH-i}$.

The translation vector of the local coordinate systems $O_{TBH-i} - X_{TBH-i} Y_{TBH-i} Z_{TBH-i}$ with the global coordinate system $O_{TBH} - X_{TBH} Y_{TBH} Z_{TBH}$ transformation is t_{TBH} .

$$t_{TBH} = (x_{TBH}, y_{TBH}, z_{TBH}) \quad (25)$$

The antisymmetric matrix of the translation vector is:

$$T_{TBH} = \begin{bmatrix} 0 & -z_{TBH} & y_{TBH} \\ z_{TBH} & 0 & -x_{TBH} \\ -y_{TBH} & x_{TBH} & 0 \end{bmatrix} \quad (26)$$

The accompanying matrix Ad of the coordinate transformation is:

$$Ad_{TBH} = \begin{bmatrix} R_{TBH} & \mathbf{0}_{3 \times 3} \\ T_{TBH} R_{TBH} & R_{TBH} \end{bmatrix}_{6 \times 6} \quad (27)$$

where $\mathbf{0}_{3 \times 3}$ is a third-order zero matrix.

For the triangular flexure hinges, the coordinate transformation satisfies:

$$R_{TBH-1} = R_{TBHX}(0) R_{TBHY}(0) R_{TBHZ}(0) \\ t_{TBH-1} = \left(0 \quad -\frac{w}{2} \quad -\frac{t}{2} \right) \quad (28)$$

$$R_{TBH-2} = R_{TBHX}(0) R_{TBHY}(0) R_{TBHZ}(\pi) \\ t_{TBH-2} = \left(0 \quad \frac{w}{2} \quad -\frac{t}{2} \right) \quad (29)$$

$$R_{TBH-3} = R_{TBHX}(\pi) R_{TBHY}(0) R_{TBHZ}\left(\frac{\pi}{2}\right) \\ t_{TBH-3} = \left(\frac{w}{2} \quad 0 \quad -\frac{t}{2} \right) \quad (30)$$

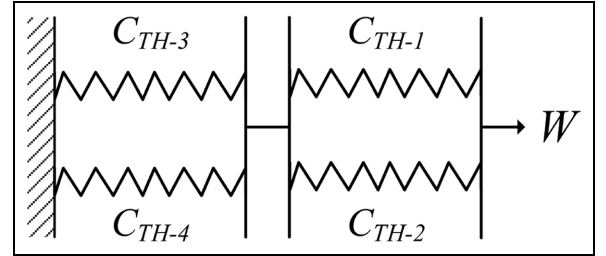


Figure 6. Equivalent force model of the hinge.

$$R_{TBH-3} = R_{TBHX}(\pi) R_{TBHY}(0) R_{TBHZ}\left(-\frac{\pi}{2}\right) \\ t_{TBH-3} = \left(\frac{w}{2} \quad 0 \quad -\frac{t}{2} \right) \quad (31)$$

The triangular bi-axial flexure hinge consists of four triangular flexure hinges that is firstly connected in parallel and then in series. According to the spring series-parallel principle,³⁶ the model of equal effectiveness is shown in Figure 6, so its flexibility matrix C_{TBH} is:

$$C_{TBH} = \left((Ad_{TBH-1} C_{TH} Ad_{TBH-1}^T)^{-1} + (Ad_{TBH-2} C_{TH} Ad_{TBH-2}^T)^{-1} \right)^{-1} \\ + \left((Ad_{TBH-3} C_{TH} Ad_{TBH-3}^T)^{-1} + (Ad_{TBH-4} C_{TH} Ad_{TBH-4}^T)^{-1} \right)^{-1} \quad (32)$$

The flexibility matrix of the triangular flexure hinge C_{TBH} can be calculated as follows:

$$C_{TBH} = \begin{bmatrix} c_{TBH-11} & 0 & 0 & 0 & c_{TBH-15} & 0 \\ 0 & c_{TBH-22} & 0 & c_{TBH-24} & 0 & 0 \\ 0 & 0 & c_{TBH-33} & 0 & 0 & 0 \\ 0 & c_{TBH-42} & 0 & c_{TBH-44} & 0 & 0 \\ c_{TBH-51} & 0 & 0 & 0 & c_{TBH-55} & 0 \\ 0 & 0 & 0 & 0 & 0 & c_{TBH-66} \end{bmatrix} \quad (33)$$

The elements in C_{TBH} are:

$$c_{TBH-11} = c_{TBH-22} = \frac{3L(L^2 + h^2)}{Eb(4L^2h^2 + h^4)} + \frac{12L^3(v+1)}{Eb(3L^2b^2 + L^2h^2 + 6L^2w^2 + 6h^2w^2 + 2L^2b^2v + 6L^2vw^2 + 6h^2vw^2)} \quad (34)$$

$$c_{TBH-15} = c_{TH-51} = \frac{3L(\sqrt{2}L^3 - 2L^2t + \sqrt{2}L^3v - 2L^2tv)}{Eb(3L^2b^2 + L^2h^2 + 6L^2w^2 + 6h^2w^2 + 2L^2b^2v + 6L^2vw^2 + 6h^2vw^2)} - \frac{3L(tL^2 + \sqrt{2}Lh^2 + th^2)}{2Eb(4L^2h^2 + h^4)} \quad (35)$$

$$c_{TBH-24} = c_{TH-42} = \frac{3L(\sqrt{2}L^3 + 2L^2t + \sqrt{2}L^3v + 2L^2tv)}{Eb(3L^2b^2 + L^2h^2 + 6L^2w^2 + 6h^2w^2 + 2L^2b^2v + 6L^2vw^2 + 6h^2vw^2)} + \frac{3L(tL^2 - \sqrt{2}Lh^2 + th^2)}{2Eb(4L^2h^2 + h^4)} \quad (36)$$

$$c_{TBH-33} = \frac{24L^3(v+1)}{Eb(L^2h^3 + 6h^3w^2 + 9L^2b^2h + 6L^2hw^2 + 6h^3vw^2 + 8L^2b^2hv + 6L^2hvw^2)} \quad (37)$$

$$c_{TBH-44} = \frac{L(8L^2h^2 + 3L^2t^2 - 6\sqrt{2}Lh^2t + 3h^2t^2)}{4Eb(4L^2h^2 + h^4)} + \frac{L(9L^4b^2 + L^4h^2 + 6L^4w^2 + 8L^4b^2v + 6L^4vw^2 + 12L^2b^2t^2 + 6L^2h^2w^2 + 12L^2b^2tv + 6L^2h^2vw^2 + 12\sqrt{2}L^3b^2t + 12\sqrt{2}L^3b^2tv)}{4Eb^3h(3L^2b^2 + L^2h^2 + 6L^2w^2 + 6h^2w^2 + 2L^2b^2v + 6L^2vw^2 + 6h^2vw^2)} \quad (38)$$

$$c_{TBH-55} = \frac{L(8L^2h^2 + 3L^2t^2 + 6\sqrt{2}Lh^2t + 3h^2t^2)}{4Eb(4L^2h^2 + h^4)} + \frac{L^3(9L^2b^2 + L^2h^2 + 6L^2w^2 + 12b^2t^2 + 6h^2w^2 + 8L^2b^2v + 6L^2vw^2 + 12b^2tv + 6h^2vw^2 - 12\sqrt{2}Lb^2t - 12\sqrt{2}Lb^2tv)}{4Eb^3h(3L^2b^2 + L^2h^2 + 6L^2w^2 + 6h^2w^2 + 2L^2b^2v + 6L^2vw^2 + 6h^2vw^2)} \quad (39)$$

$$c_{TBH-66} = \frac{L^3}{Eb(bL^2 + bh^2)} \quad (40)$$

The rotational stiffness of the triangular bi-axial flexure hinge in the x -axis and y -axis directions are:

$$K_{M_x-\theta_x} = K_{M_y-\theta_y} = \frac{1}{c_{TBH-11}} = \frac{1}{c_{TBH-22}} \quad (41)$$

Equation (41) shows that the length L , height h , and width b of the hinge all have effects on the stiffness of the triangular bi-axial flexure hinge. Figure 7 shows the effect of variables L , h , and b on rotational stiffness for a given E , t , and w . It can be seen from Figure 7 that when h is fixed, the rotational stiffness

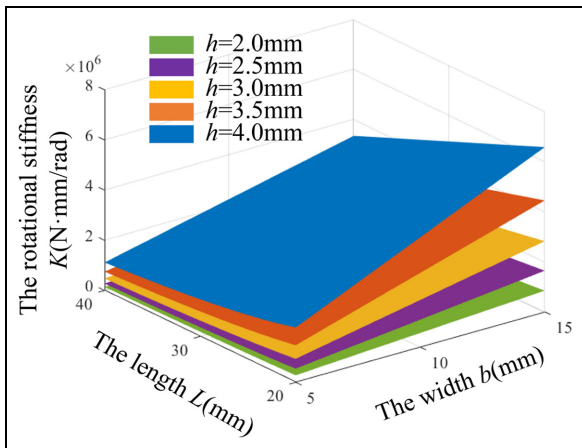


Figure 7. Variation of rotational stiffness K with respect to design variables L , h , and b .

K increases as L decreases and b increases, and the change is essentially the same. And as h is increasing, K is likewise increasing.

Analysis of the triangular bi-axial flexure hinge

In this section, a finite element model was built to analyze the hinge. The initial hinge parameters were $h = 3.0$ mm, $L = 27.5$ mm, $b = 10$ mm, $t = 100$ mm, and $w = 60$ mm. The material of the hinge had an elastic modulus E of 106,820 MPa and Poisson's ratio ν of 0.34. The flexure hinge's C3D10 mesh model was created, and as shown in Figure 8(a), the mesh's average edge length was 3 mm. In all deformation zones, detailed meshes with at least five elements per line were created to obtain accurate results even in areas of high strain concentration (Figure 8(b)).

Rotational flexibility analysis

Because the hinge is used to support an optical precision equipment, its role is equivalent to that of a universal joint. So only the elements of the flexibility matrix C_{TBH} that affect the rotational angle of the hinge around the x , y axes, that is, $c_{TBH-11}(c_{\theta_x-M_x})$, $c_{TBH-22}(c_{\theta_y-M_y})$, $c_{TBH-15}(c_{\theta_x-M_y})$, and $c_{TBH-24}(c_{\theta_y-M_x})$ are verified. The results are shown in Table 1. As can be seen from the table, the relative error is less than 4%, which verifies the correctness of the analysis model.

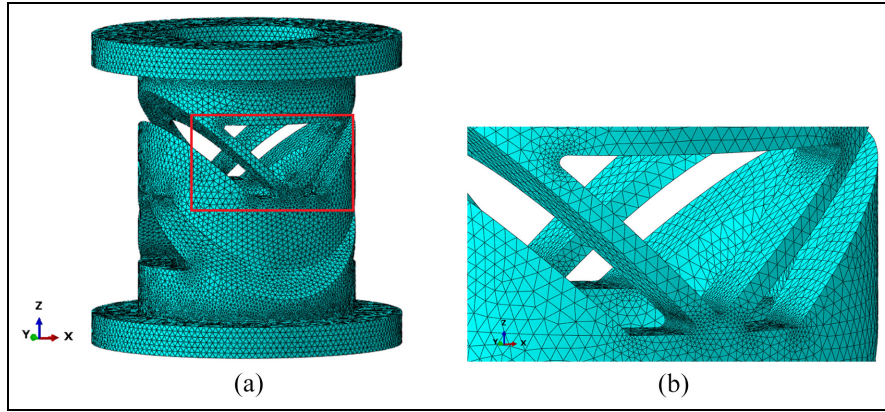


Figure 8. Finite element mesh of the hinge: (a) mesh of the FEM and (b) mesh detail in thin sections.

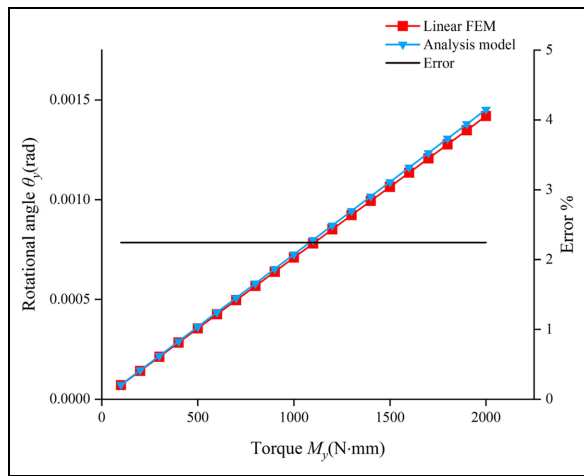


Figure 9. Comparison of analysis model and linear FEM of hinge rotational angle θ_y .

Linear and nonlinear analysis

In the small deformation analysis of the hinge, the linear angle transformation of the hinge under the torque in the y -direction was studied by using the linear finite element model. The lower platform of the flexure hinge was subject to a 6-DOF constraint as part of the finite element analysis’s boundary conditions, whereas the center of the upper platform was subject to the y -direction torque of M . Therefore, it was possible to use the FEM to determine the hinge’s rotational angle in the y -direction. The comparison between the analysis model and the linear finite element model is shown in Figure 9. The analytically calculated value closely resembled the outcome of the finite element simulation value, and the relative error was 2.3% or less.

The nonlinear problem of a structure refers to the change of its stiffness with its deformation, mainly geometric nonlinearity, material nonlinearity, and state nonlinearity. For flexure hinges, the nonlinearity in the structural response caused by large changes in geometry when subjected to large

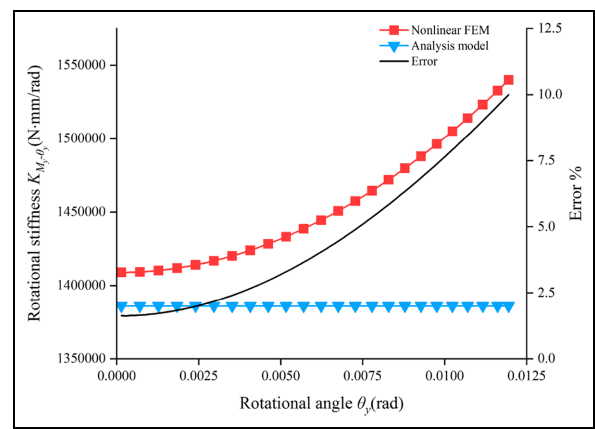


Figure 10. Comparison of analysis model and nonlinear FEM of hinge rotational stiffness $K_{\theta_y-M_y}$.

Table 1. Verification of rotational flexibility.

	Analysis (rad/N·mm)	Simulation (rad/N·mm)	Error (%)
CTBH-11	7.26E-7	7.18E-7	1.10
CTBH-22	7.26E-7	7.09E-7	2.34
CTBH-15	-3.64E-5	-3.52E-5	3.29
CTBH-24	3.63E-5	3.62E-5	0.24

deflections or rotations is geometric nonlinearity.^{18,37} In the hinge’s large deformation analysis, the nonlinear finite element model was used to study the nonlinear transformation of the rotational stiffness of the hinge with the rotational angle under the torque about the y -direction, and the rotational stiffness was compared with that of the analysis model. In Figure 10, when the torque is smaller than 12.2 (N·m), which correspond to a rotational angle of 0.0119 (rad), the rotational stiffness errors between the nonlinear finite element model and analysis models were less than 10%. When the rotational angle is less than 0.0047 (rad), the rotational stiffness error was less than 3%.

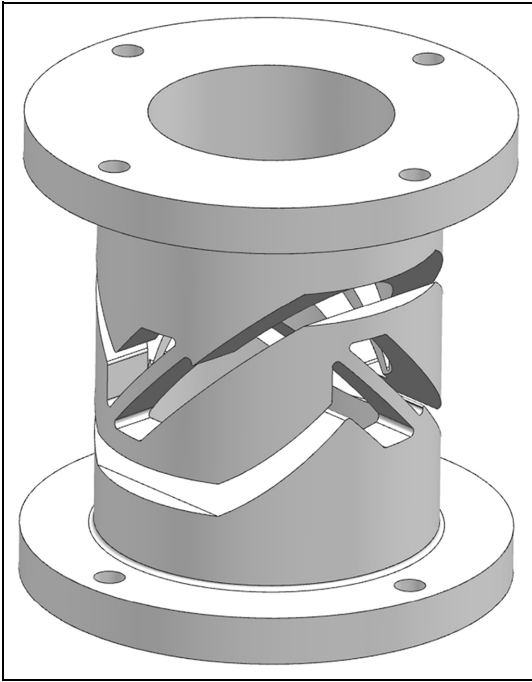


Figure 11. The cross-axis bi-axial hinge.

Comparison with the cross-axis flexure hinge

Compared to the cross-axis flexure hinge, which is also a compact hinge, the triangular hinge has a limited range of motion. Since the designed hinge is used for supporting an optical precision equipment, high precision is required for the hinge rotation, while there is less requirement for the range of motion. The nonlinear finite element method was used to compare the rotational capacity and center drift of the triangular bi-axial hinge and the cross-axis bi-axial hinge, respectively. The cross-axis bi-axial hinge is shown in Figure 11, and its flexible unit is the same size as the triangular bi-axial hinge.

A series of bending torques about the y -direction were applied to the top center of the triangular bi-axial hinge and the cross-axis bi-axial hinge respectively, and the corresponding rotational angles are shown in Figure 12. As can be seen from the figure, the rotational angle of the cross-axis bi-axial hinge is more than six times than that of the triangular bi-axial hinge when subjected to the same torque. And it can be seen that with the increase of torque, the rotational angle of the cross-axis bi-axial hinge shows a significant nonlinearity phenomenon. The finite element simulation results confirm that the use of the triangular hinge will lead to a limited motion range compared with the cross-axis hinge.

Figure 13 shows the corresponding center drift of the hinge at the different rotational angles. As can be seen from the figure, the center drift of both hinges increases as the rotational angle increases. The cross-axis bi-axial hinge has more than 3.7 times as much center drift as the triangular bi-axial hinge when

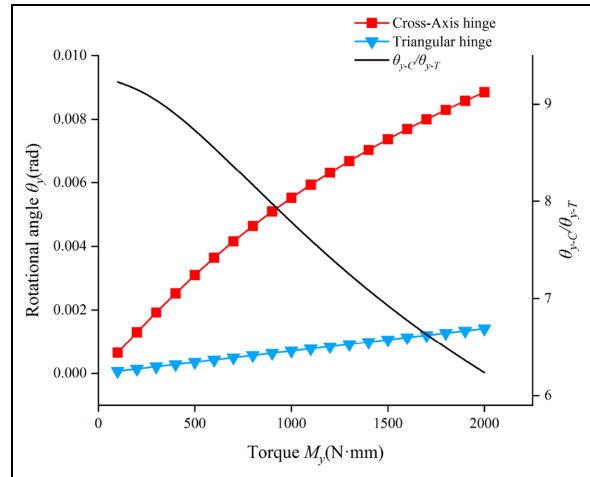


Figure 12. Rotational angles at different torques.

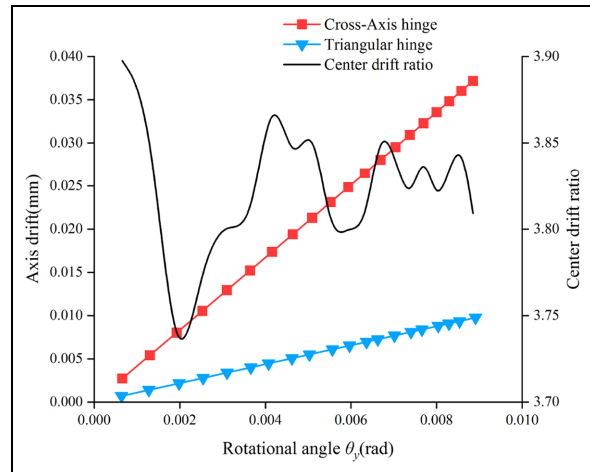


Figure 13. Center drift at different rotational angles.

rotated at the same angle about the y -direction. The finite element simulation results confirm that the triangular hinge has higher motion precision than the cross-axis hinge.

The results of the nonlinear finite element method show that for structure we designed, the cross-axis bi-axial hinge has high rotational capacity and the triangular bi-axial hinge has high rotational accuracy. Since the hinge is used for supporting an optical precision equipment, the triangular bi-axial hinge is more suitable compared to the cross-axis bi-axial hinge.

Optimization of the triangular bi-axial flexure hinge

To determine the flexure hinge design that meets the requirements and has the best performance, it is necessary to determine the optimal values of h and L . According to the handbook of metal properties, TC4 (Ti-6Al-4V) has the advantages of low density, high strength, high specific stiffness, low expansion

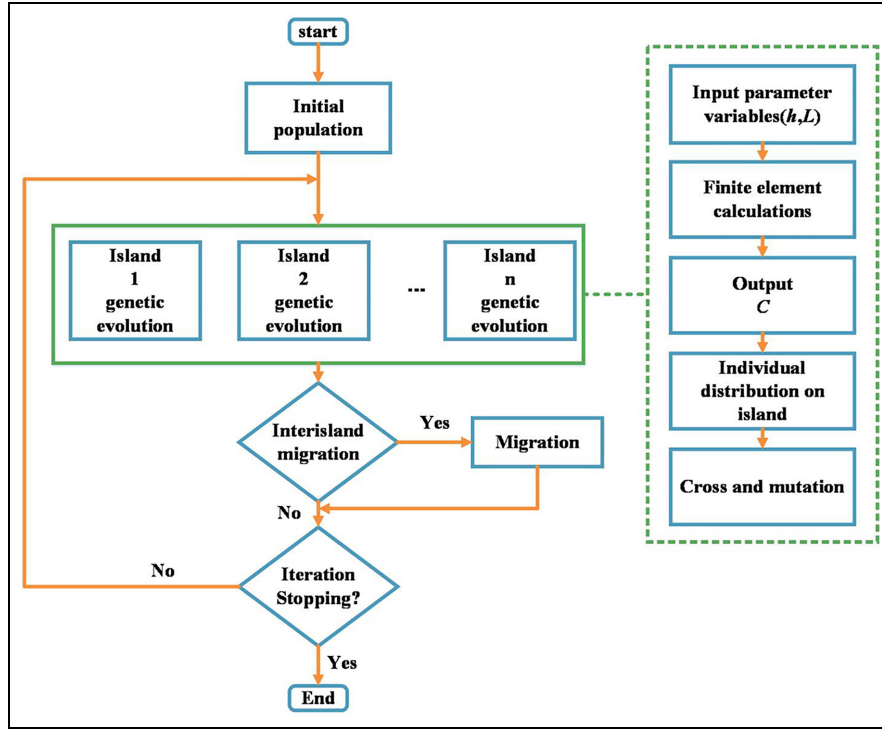


Figure 14. Geometric parameter optimization process.

coefficient, and good mechanical properties. Therefore, titanium alloy TC4 was chosen as the hinge material, whose modulus of elasticity is 106,820 MPa, Poisson's ratio is 0.34, density is 4.51 g/cm³, and yield strength is 895 MPa.

Many researchers have applied algorithms to the structural optimization of flexure mechanisms.^{38,39} For the triangular bi-axial flexure hinge, the general expression of the optimized mathematical model is as follows:

$$\text{find} \begin{cases} \max \theta(h, L) \\ \min d(h, L) \end{cases} \quad (42)$$

$$\text{s.t.} \begin{cases} 2.5\text{mm} \leq h \leq 3.5\text{mm} \\ 25\text{mm} \leq L \leq 30\text{mm} \end{cases} \quad (43)$$

where $\theta(h, L)$ is the rotation angle of the flexure hinge subjected to a bending moment and $d(h, L)$ is the center drift of the hinge rotation axis under the same moment.

To simplify the optimization algorithm, the dimensionless number C is designated. The maximal rotation angle θ and minimal center drift d are achieved by maximizing C :

$$C = \frac{\theta(h, L)}{d(h, L)} \quad (44)$$

The geometric parameter optimization process is shown in Figure 14. This algorithm use the same FEM as that in Section "Analysis of the triangular bi-axial flexure hinge," with element type C3D10.

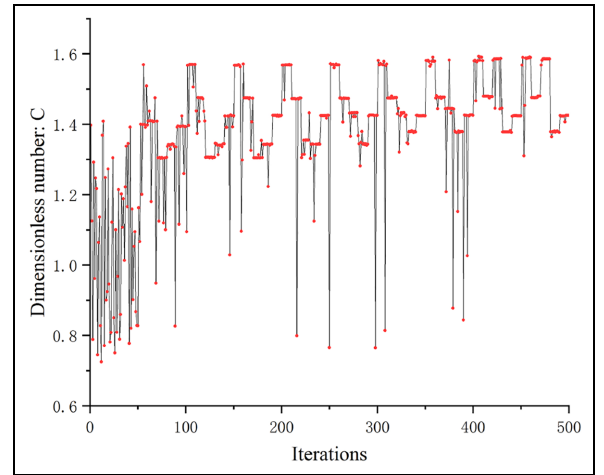


Figure 15. Optimization process.

The torque is applied to the top center of the hinge with a magnitude of 1000 N-mm and a direction parallel to the rotation axis.

Compared with traditional optimization algorithms, the multi-island genetic algorithm has superior computational efficiency, better global search capability, and avoids local optimal solutions.^{40,41} Multiple subpopulations are created by MIGA from a large population. Subpopulation evolution results from genetic manipulation. Additionally, an elite retention strategy is used to guarantee that the best traits of the parents are passed on to the progeny. For migration operations, multi-island genetic algorithms typically

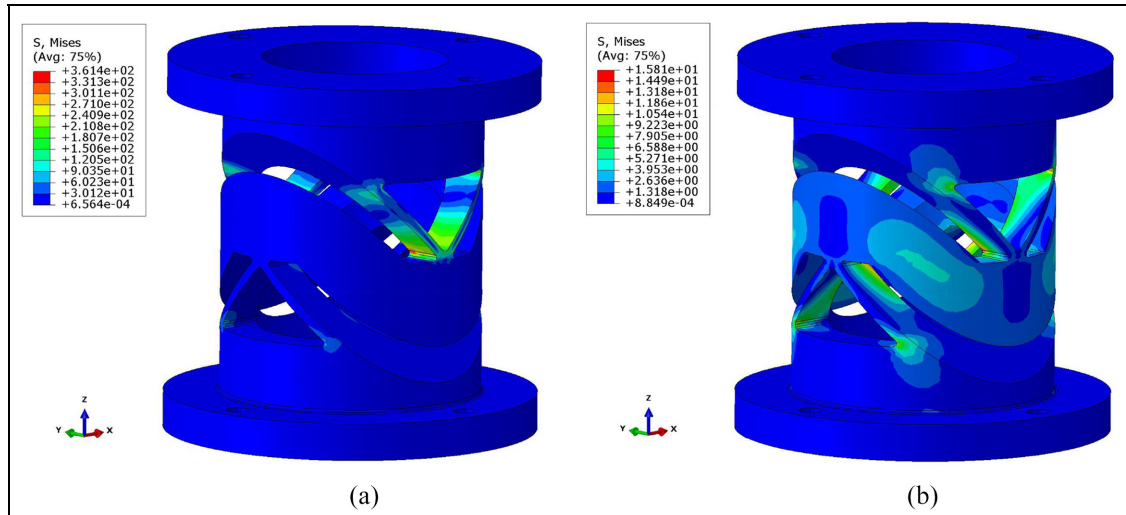


Figure 16. Results of the static simulation: (a) force in the x -direction and (b) force in the z -direction.

Table 2. Results before and after optimization.

	Before optimization	After optimization	Relative change (%)
Geometrical parameters (10^{-4} mm)	$h = 3.0$, $L = 27.5$	$h = 2.5$, $L = 25.3$	
Rotation angle (10^{-4} rad)	6.97	10.39	49.1
Center drift (10^{-4} mm)	6.89	6.52	5.4
C	1.01	1.59	57.4

randomly choose some individuals and move them to other islands. This preserves the population's diversity and avoids local optimal solutions as much as possible. Hence, in this study, MIGA was used to optimize the geometrical parameters. The subpopulation size was 10, the number of islands was 5, the number of generations was 10, and the rate of crossover was 1.0. The initial geometrical parameters were $h = 3.0$ mm and $L = 27.5$ mm. After 500 iterations of the optimization process, the geometrical parameters were $h = 2.5$ mm and $L = 25.3$ mm. Figure 15 shows the optimization process. Each red point in the graph corresponds to an optimal solution. Table 2 shows the results both before and after optimization. All calculations are conducted on a desktop PC (CPU frequency: 2.60 GHz, RAM: 16 GB) with 64-bit Windows 10 operating system. The computational time of 500 iterations is 4 h and 10 min.

Table 2 shows that optimizing the geometrical parameters of the flexure hinge resulted in the rotation angle improving by 49.1%, the center drift reducing by 5.4%, and the dimensionless number C increasing by 57.4%. This indicates that, using MIGA, the rotational stiffness and rotational accuracy of the hinge were effectively enhanced.

Mechanical analysis

As a result of the structural design in Section "Triangular bi-axial flexure hinge analysis model," in addition to dimensional optimization in Section "Optimization of the triangular bi-axial flexure hinge," the flexure hinge configuration was finally determined. To verify its compliance with the requirements, it had to undergo static analysis and modal analysis.

Static analysis

Considering the influence of the mass of the optical instrument, the entire bottom of the flexure hinge was fixed and 280 N of force was applied along the x or z -direction at the top center to simulate the vertical or horizontal placement of the optical instrument (Figure 16).

As shown in Figure 16(a), in the case of vertical placement, the maximum stress area was at the top of the triangular area of the hinge and the maximum stress was 361.4 MPa. From Figure 16(b), in the case of horizontal placement, the maximum stress area was also at the top of the triangular area of the hinge and the maximum stress was 5.646 MPa. Under these two conditions, the stress of the hinge was much less than the ultimate yield stress of the titanium alloy TC4 (895 MPa). Hence, in the structural design, the strength of the hinge met the requirements.

Modal analysis

The system's dynamic performance is reflected in the system's modal shape and modal frequency. Because the hinge is used to support optical precision equipment, it is affected by a series of complex scenarios, such as vibration and noise during transportation and use, and the hinge requires sufficient mechanical

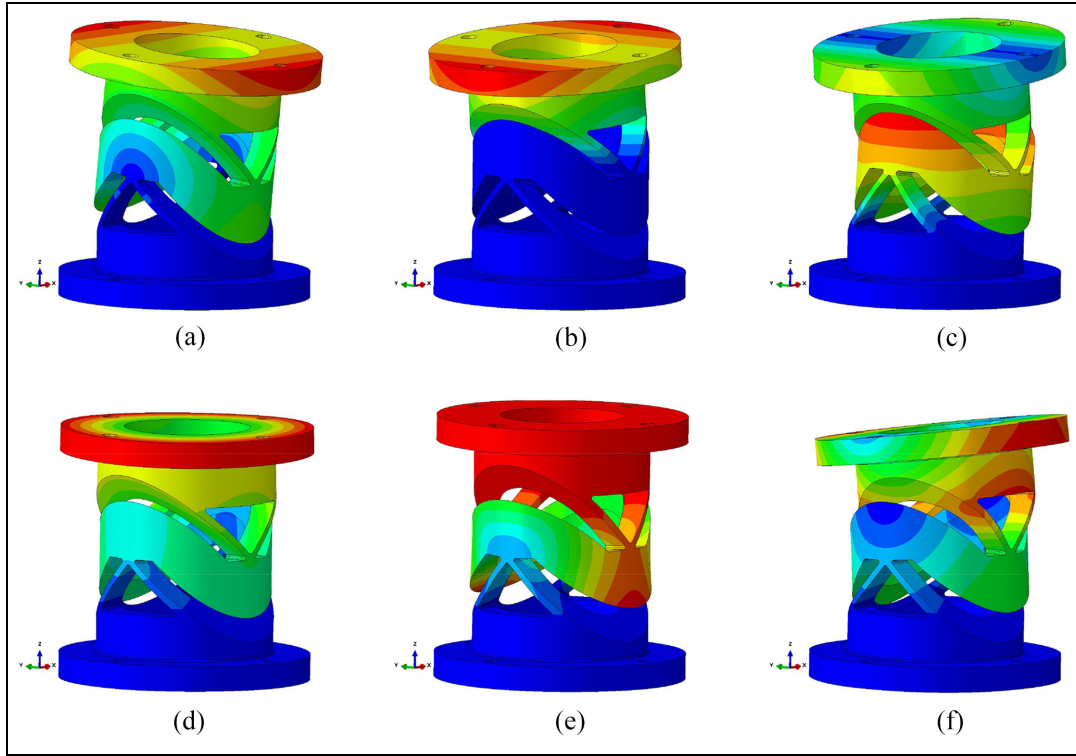


Figure 17. Simulation results for the modals: (a) first mode, (b) second mode, (c) third mode, (d) fourth mode, (e) fifth mode, and (f) sixth mode.

performance to ensure its safety. The second-order dynamic equilibrium equation is usually used for the modal analysis of the mechanical structure:

$$[M]\{\ddot{x}(t)\} + [C]\{\dot{x}(t)\} + [K]\{x(t)\} = F(t) \quad (45)$$

where $[M]$ is the mass matrix, $[C]$ is the damping matrix, $[K]$ is the stiffness matrix, $\{\ddot{x}(t)\}$ is the externally excited acceleration signal, $\{\dot{x}(t)\}$ is the externally excited velocity signal, $\{x(t)\}$ is the externally excited displacement signal, and $F(t)$ is the external load.

When no external load is applied and damping has little effect on the modal frequency and modal shape of the mechanical structure, the damping matrix of the mechanical system can be ignored. Equation (45) can be transformed into the dynamic equation of undamped free vibration:

$$[M]\{\ddot{x}(t)\} + [K]\{x(t)\} = 0 \quad (46)$$

The free vibration of the mechanical structure is simple harmonic motion, but its displacement is a sinusoidal function:

$$\{x\} = \{\phi\}_i \cos(\omega_i t) \quad (47)$$

$\{\phi\}_i$ denotes the eigenvectors of the i -th order modal vibration, ω_i is the inherent frequency of the i -th order mode, and t is time.

Substituting equation (47) into equation (46) yields:

$$([K] - \omega_i^2[M])\{\phi\}_i = 0 \quad (48)$$

Because the amplitude of each node cannot be zero, the coefficient determinant in equation (48) must be zero; hence, the free vibration equation of the mechanical structure can be obtained as follows:

$$|[K] - \omega_i[M]| = 0 \quad (49)$$

For mechanical structures with N DOFs, the natural frequencies of the N orders can be obtained using equation (49), and the modal shapes of the corresponding orders can be obtained by substituting them into equation (48).

The modal superposition procedure was used in this study's modal analysis of the triangular bi-axial flexure hinge. First, the FEM in Section 4 "Analysis of the triangular bi-axial flexure hinge" was used to divide the coarse mesh and fine mesh, and then the boundary constraints were applied to simulate the mechanical resonant frequency of the hinge.

The first six modes of the triangular bi-axial flexure hinge are shown in Figure 17. The figure shows that the first mode rotated around the x -axis, the second mode rotated around the y -axis, the third mode was translational along the x -axis, the fourth mode rotated around the z -axis, the fifth mode was

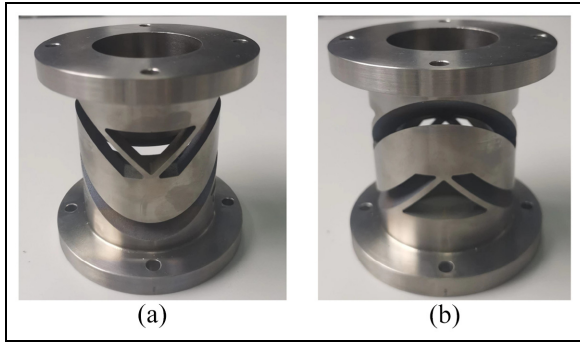


Figure 18. Physical view of the triangular bi-axial flexure hinge: (a) front view and (b) side view.

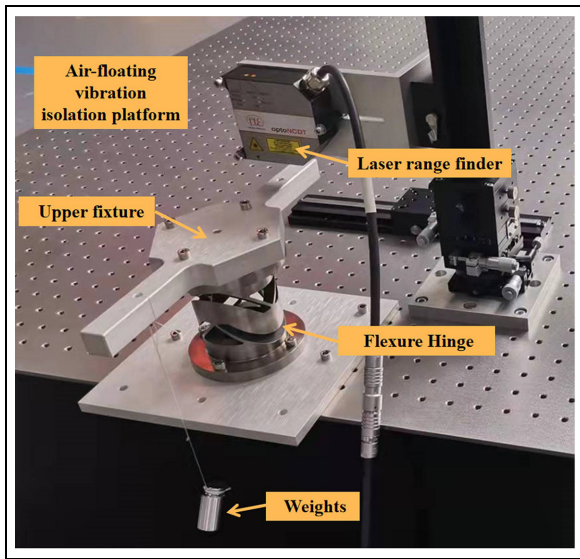


Figure 19. Test system.

translational along the z -axis, and the sixth mode was translational along the y -axis.

The first six orders of modal frequencies and the modal shape of the triangular bi-axial flexure hinge are shown in Table 3, where the first and second-order simulation results are mechanical resonant frequencies in the working direction and the last four orders are mechanical frequencies in the non-working direction.

The first and second inherent frequencies of the hinge were 152.1 and 156.8 Hz, respectively, according to the finite element modal analysis. The hinge's structural dynamic stiffness, which surpassed the design index requirements that the natural frequency be larger than 150 Hz, is reflected in these frequencies. This means that the hinge did not resonate with other structural parts of the optical precision equipment.

The physical hinge is shown in Figure 18.

Testing

Rotational stiffness

A test system was built, as illustrated in Figure 19, to evaluate the accuracy of the stiffness equation and

Table 3. Modal analysis results.

Modal order	Modal frequency (Hz)	Modal shape
1	152.1	Rotate around x
2	156.8	Rotate around y
3	1190.7	x direction
4	1269.3	Rotate around z
5	1294.3	z direction
6	1606.2	y direction

Table 4. Rotation angle experimental data.

Number of measurements	Weight mass M (g)	The angle of rotation (β 10^{-5} rad)	The rotational stiffness K_M (N·m)
1	100	8.8	1114.3
2	200	16.6	1181.5
3	300	29.9	983.9
4	400	44.4	883.4
5	500	54.4	901.3
6	600	64.4	913.6
7	700	77.8	882.3
8	800	89.9	872.6
9	900	101.1	872.9
10	1000	114.4	857.2
11	1100	126.6	852.1
12	1200	138.9	847.2
Average value			930.9

simulation optimization findings. The precise experimental approach is as follows: To simulate the torque applied to the hinge, a metal weight of mass M was suspended in the upper fixture at a distance of 0.1 m from the hinge's center axis. A laser range finder was used to measure the triangular bi-axial flexure hinge's vertical displacement z when the hinge was subjected to simulated torque. The following equation can be used to determine the rotation's angle β :

$$\beta = \frac{\pi \arctan(\frac{z}{r})}{180^\circ} \quad (50)$$

where r is the distance between the measuring point of the laser range finder and the center of the hinge; its value was 100 mm. All experimental equipment was placed on an air-floating vibration isolation platform to isolate external vibration. The metal weight used in the experiment started off at a mass of 100 g, and changed in the rotation angle of the flexure hinge were monitored in increments of 100 g up until 1200 g.

The results are shown in Table 4. Then the experimentally measured value of the rotational stiffness K_M of the triangular bi-axial flexure hinge was derived from

$$K_M = \frac{Mgl}{\beta} \quad (51)$$

where $g = 9.8 \text{ m/s}^2$ and $l = 0.1 \text{ m}$.

Table 5. Comparison of rotational stiffnesses.

Rotational stiffness K_M (N·m/rad)	Analysis	Simulation	Experimental
	869.6	934.6	930.9

Table 5 shows a comparison of the three results for the triangular bi-axial flexure hinge's analytically calculated value (calculated using analysis model), simulated calculated value, and experimental value. The maximal relative error between them was 6.95%. This result verifies the accuracy of the derived analytical formula and simulation optimization results.

Error analysis

Table 5 shows that the maximum relative error between the analytically calculated value, simulated calculated value, and experimental value was 6.95%. It is imperative to analyze the source of the error. First, the cantilever beam stress-strain model was simplified in the process of deriving the hinge rotational stiffness equation. The hinge deformation in the real case was more complex; hence, simplification introduced model errors. Second, during the finite element analysis, a discrete approximation of the continuum was used in the computation. The type and size of the element had an impact on the quality of the calculation, which eventually resulted in discrete mistakes. Additionally, the numerical computation method was applied to resolve the finite element problem; however, it approximated the actual analytical solution and introduced errors. Finally, during the measurement experiment, the surface roughness of the upper fixture caused errors in the laser range finder during the measurement of the displacement of the hinge.

Conclusions

To achieve the requirement of flexure hinges for specific optical precision equipment, in this study, a new triangular bi-axial flexure hinge was proposed, the analysis model for the flexibility of the triangular bi-axial flexure hinges was derived, for and the effect of hinge length L , hinge height h , and hinge width b on rotational stiffness were investigated. After that, the linear and nonlinear finite element methods were used to verify the analysis model, the designed hinge was compared with the cross-axis bi-axial hinge. Then, the hinge geometry was optimized using the multi-island genetic algorithm, which improved the rotation angle by 49.1% and reduced center drift by 5.4%. Next, static and modal analyses of the hinges were conducted. Finally, a test system was constructed to measure the flexure hinge's rotation angle and rotational stiffness. The results demonstrated that the analytically calculated value was 869.6 N·m/rad, simulated

calculated value was 934.6 N·m/rad, and experimental value was 930.9 N·m/rad, and the maximum relative error between the three was 6.95%. Then three aspects of the error sources were analyzed. In conclusion, the analysis model met the requirements of the design of hinges, and the use of the multi-island genetic algorithm effectively optimized the hinge parameters and improved its performance. The design of triangular bi-axial flexure hinges provides new ideas for other structural forms of hinges.


Declaration of conflicting interests


The author(s) declared no potential conflicts of interest with respect to the research, authorship, and/or publication of this article.


Funding

The author(s) disclosed receipt of the following financial support for the research, authorship, and/or publication of this article: This work was supported by the National Natural Science Foundation of China [Grant No. 52005478].

ORCID iDs

Jun-wei Lin  <https://orcid.org/0000-0002-6638-5084>

Yang Zhao  <https://orcid.org/0000-0002-1492-6459>

Ha-si-ao-qi-er Han  <https://orcid.org/0000-0002-8427-3377>

References

- Chandrasekaran K and Thondiyath A. Design of a two degree-of-freedom compliant tool tip for a hand-held powered surgical tool. *J Med Device* 2017; 11(1): 014502.
- Wu J, Zhang Y, Lu Y, et al. Modeling and design of a two-axis elliptical notch flexure hinge. *Rev Sci Instrum* 2018; 89(4): 045010.
- Du S, Liu J, Bu H, et al. A novel design of a high-performance flexure hinge with reverse parallel connection multiple-cross-springs. *Rev Sci Instrum* 2020; 91(3): 035121.
- Ma W, Wang R, Zhou X, et al. The performance comparison of typical notched flexure hinges. *Proc IMechE, Part C: J Mechanical Engineering Science* 2020; 234(9): 1859–1867.
- Zhang L, Wang T, Zhang F, et al. Design and optimization of integrated flexure mounts for unloading lateral gravity of a lightweight mirror for space application. *Appl Opt* 2021; 60: 417–426.
- Yang FF, Tian HY, Yan CX, et al. Athermal design of the mirror support with flexure hinges for the laser communication terminal. *Optoelectron Lett* 2019; 15(6): 454–458.
- Sun X, Yang B, Gao Y, et al. Integrated design, fabrication, and experimental study of a parallel micro-nano positioning-vibration isolation stage. *Robot Comput Integr Manuf* 2020; 66: 101988.
- Ning P, Xia X, Qiao G, et al. A dual-mode excitation method of flexure hinge type piezoelectric stick-slip

- actuator for suppressing backward motion. *Sens Actuators A Phys* 2021; 330: 112853.
9. Li J, Chen S, Zhao G, et al. A linear piezoelectric actuator with the parasitic motion of equilateral triangle flexure mechanism. *Smart Mater Struct* 2020; 29(1): 015015.
 10. Gräser P, Linß S, Harfensteller F, et al. High-precision and large-stroke XY micropositioning stage based on serially arranged compliant mechanisms with flexure hinges. *Precis Eng* 2021; 72: 469–479.
 11. Wang P and Xu Q. Design of a flexure-based constant-force XY precision positioning stage. *Mech Mach Theory* 2017; 108: 1–13.
 12. Huo Z, Tian Y, Wang F, et al. A dual-driven high precision rotary platform based on stick-slip principle. *IEEE/ASME Trans Mechatron* 2022; 27: 3053–3064.
 13. Yan B and Liang L. A novel fiber Bragg grating accelerometer based on parallel double flexible hinges. *IEEE Sens J* 2020; 20(9): 4713–4718.
 14. Farhadi Machekposhti D, Tolou N and Herder JL. A review on compliant joints and rigid-body constant velocity universal joints toward the design of compliant homokinetic couplings. *J Mech Des* 2015; 137(3): 032301.
 15. Tian Y, Shirinzadeh B, Zhang D, et al. Three flexure hinges for compliant mechanism designs based on dimensionless graph analysis. *Precis Eng* 2010; 34(1): 92–100.
 16. Lobontiu N. *Compliant mechanisms: design of flexure hinges*. Milton: Taylor & Francis Group, 2021.
 17. Jingjun Y, Xu P, Minglei S, et al. A new large-stroke compliant joint & micro/nano positioner design based on compliant building blocks. In *2009 ASME/IFTOMM international conference on reconfigurable mechanisms and robots*, pp.409–416. Genova, Italy
 18. Palmieri G, Palpacelli MC and Callegari M. Study of a fully compliant U-joint designed for minirobotics applications. *J Mech Des* 2012; 134(11): 111003.
 19. Tanik E and Parlaktaş V. Compliant cardan universal joint. *J Mech Des* 2012; 134(2): 021011.
 20. Li L, Zhang D, Qu H, et al. Generalized model and configuration design of multiple-axis flexure hinges. *Mech Mach Theory* 2022; 169: 104677.
 21. Trease BP, Moon YM and Kota S. Design of large-displacement compliant joints. *J Mech Des* 2005; 127(4): 788–798.
 22. Choi YJ, Sreenivasan SV and Choi BJ. Kinematic design of large displacement precision XY positioning stage by using cross strip flexure joints and over-constrained mechanism. *Mech Mach Theory* 2008; 43(6): 724–737.
 23. Lobontiu N, Paine JSN, Garcia E, et al. Design of symmetric conic-section flexure hinges based on closed-form compliance equations. *Mech Mach Theory* 2002; 37(5): 477–498.
 24. Yu JJ, Pei X, Li SZ, et al. Type synthesis principle and practice of flexure systems in the framework of screw theory: part II—numerations and synthesis of complex flexible joints. In: *ASME 2010 international design engineering technical conferences and computers and information in engineering conference*, pp.553–561. New York, USA
 25. Dirksen F and Lammering R. On mechanical properties of planar flexure hinges of compliant mechanisms. *Mech Sci* 2011; 2(1): 109–117.
 26. Shusheng B, Shanshan Z and Xiaofeng Z. Dimensionless design graphs for three types of annulus-shaped flexure hinges. *Precis Eng* 2010; 34(3): 659–666.
 27. Mahto S. Shape optimization of revolute-jointed single link flexible manipulator for vibration suppression. *Mech Mach Theory* 2014; 75: 150–160.
 28. Pei X, Yu J, Zong G, et al. A novel family of leaf-type compliant joints: combination of two isosceles-trapezoidal flexural pivots. *J Mech Robot* 2009; 1(2): 021005.
 29. Ling M, Howell LL, Cao J, et al. A pseudo-static model for dynamic analysis on frequency domain of distributed compliant mechanisms. *J Mech Robot* 2018; 10(5): 051011.
 30. Chen Z, Chen G and Zhang X. Damped leaf flexure hinge. *Rev Sci Instrum* 2015; 86(5): 055002.
 31. Zhang Y, Wu J and Tan J. Compliance model and structure optimization method based on genetic algorithm for flexure hinge based on X-lattice structure. *Complexity* 2021; 2021: 1–14.
 32. Awtar S, Slocum AH and Sevincer E. Characteristics of beam-based flexure modules. *J Mech Des* 2007; 129(6): 625–639.
 33. Li S and Hao G. Design and nonlinear spatial analysis of compliant anti-buckling universal joints. *Int J Mech Sci* 2022; 219: 107111.
 34. Zhao H, Bi S and Yu J. Modeling and analysis of triangle flexible hinge. *Chin J Mech Eng* 2009; 45(8): 1–5.
 35. Selig JM and Ding X. A screw theory of timoshenko beams. *J Appl Mech* 2009; 76: 031003.
 36. An M, Zhang L, Xu S, et al. Design, analysis, and testing of kinematic mount for astronomical observation instrument used in space camera. *Rev Sci Instrum* 2016; 87(11): 114501.
 37. Li S, Hao G and Wright WMD. Design and modelling of an anti-buckling compliant universal joint with a compact configuration. *Mech Mach Theory* 2021; 156: 104162.
 38. Liu M, Zhang X and Fatikow S. Design of flexure hinges based on stress-constrained topology optimization. *Proc IMechE, Part C: J Mechanical Engineering Science* 2017; 231(24): 4635–4645.
 39. Chau NL, Tran NT and Dao TP. Topology and size optimization for a flexure hinge using an integration of SIMP, deep artificial neural network, and water cycle algorithm. *Appl Soft Comput* 2021; 113: 108031.
 40. Kushida JI, Hara A, Takahama T, et al. Island-based differential evolution with varying subpopulation size. In: *2013 IEEE 6th international workshop on computational intelligence and applications (IWCIA)*, pp.119–124, Hiroshima, Japan.
 41. Gong YJ, Chen WN, Zhan ZH, et al. Distributed evolutionary algorithms and their models: a survey of the state-of-the-art. *Appl Soft Comput* 2015; 34: 286–300.